EFFECT OF STRAW CONTENT ON SOIL COMPACTION UNDER AGRICULTURAL TRAFFIC CONDITIONS
/
秸秆含量对农业交通条件下土壤压实度的影响

Jun GUO[1,2], Xinyu CHEN*[1,4], Mengzhen SHAO[1], Yang YANG[1], Kuan QIN[3]
[1] School of Automotive Engineering, Yancheng Institute of Technology, Yancheng, Jiangsu 224051, China
[2] School of Automotive Engineering, Nantong Institute of Technology，Nantong, Jiangsu 226001, China
[3] School of Engineering, Anhui Agricultural University, Hefei, Anhui 230036, China
[4] Department of Automotive Technology, Yancheng College of Mechatronic Technology, Yancheng, Jiangsu 224006, China
E-mail: cxy_1115608@163.com
DOI: https://doi.org/10.35633/inmateh-77-05

Keywords: *Soil compaction; discrete element; compressive force; soil settlement; agricultural machinery*

ABSTRACT
Soil compaction caused by agricultural machinery operations is becoming increasingly serious, damaging soil structure and affecting sustainable agricultural production. However, there has been a lack of systematic research on the quantitative effects of straw on soil compaction. Therefore, this study used the discrete element method to investigate the effects of different straw contents (0–50%) on soil compaction characteristics. The results showed that: (1) When the loading plate sinks at a constant speed of 0.01 m/s, the compressive force on the soil mixture at depths of 50 mm, 100 mm, and 150 mm with 50% straw content is reduced by 669.03 N, 639.79 N, and 382.04 N, respectively, compared to pure soil; (2) When the loading plate was applied with a constant load of 100 N, the compressive forces at the same depths were reduced by 1,289.36 N, 862.9 N, and 607.49 N, respectively. Furthermore, both simulation results and indoor compaction experiments indicate that settlement decreases with increasing straw content. Pore ratio analysis confirms that the "micro-spring" effect of straw can improve soil compressive strength. This study provides guidance for enhancing agricultural machinery mobility and mitigating soil compaction hazards.

摘要
农业机械作业导致的土壤压实问题日益严重，破坏土壤结构并影响农业可持续生产，而当前对秸秆改良土壤压实的量化效应缺乏系统探究。因此本文采用离散元法研究了不同秸秆含量（0-50%）对土壤压实特性的影响。结果表明：（1）加载板以恒定速度 0.01 m/s 下沉，得到 50%秸秆含量时 50mm、100mm 和 150mm 深度处的土壤混合体所受压缩力较纯土壤分别降低 669.03N、639.79N 和 382.04N；（2）加载板以恒定载荷 100N 作用，得到相同深度处的压缩力分别降低 1289.36N、862.9N、607.49N。其次，仿真结果与室内压实实验均表明沉陷量随秸秆含量的增加呈递减趋势，孔隙比分析验证了秸秆 "微弹簧"效应可改善土壤抗压性能。本研究对提升农业机械通过性能、减轻土壤压实危害具有指导意义。

INTRODUCTION
The movement of agricultural machinery can lead to severe soil compaction, particularly with repeated field operations (such as plowing, sowing, and spraying), which exacerbates soil compaction*(Hamza et al., 2005*). Previous studies have primarily focused on reducing soil compaction by lowering tire inflation pressure and increasing vehicle speed, with common approaches involving reducing load or increasing contact area. For example, *Moslem et al., (2014)*, used SolidWorks Simulation to create a 3D model of radial tires, analyzing the impact of tire inflation pressure and axial load on soil compaction. *Gheshlaghi et al., (2020*), compared the finite element method with the Bekker and Wismer-Luth models to study the interaction between clay loam and agricultural tires, as well as the effect of vertical load on rolling resistance. While finite element methods can effectively simulate post-compaction soil deformation, they struggle to accurately describe local soil failure and particle flow due to the discrete nature of soil and straw particles. Research on the complex interactions between straw and soil compaction, as well as the force and compression characteristics of straw-soil mixtures under external forces, remains limited.

The application of the Discrete Element Method (DEM) to study force transmission in cultivated soils remains limited to recent research; for example, when DEM Elasto-plastic models are optimized for soil–bulldozer blade interaction, large prediction errors in force–displacement–energy arise, yet a Pareto-optimal solution can ultimately be obtained (*Abdeldayem, et al., 2025*).

Jjagwe et al., (2023), developed a simplified model grounded in the scaling law of the pressure–sinkage relationship and refined it with a normalized correction coefficient, thereby reducing the prediction error in soil-compression resistance to within acceptable limits. This advancement significantly enhances the precision of tire-induced soil compaction control. Additionally, researchers have experimentally developed a DEM model for the straw-soil composite, capable of simulating dynamic characteristics such as soil displacement, straw displacement, velocity, movement trajectories, and residue burial (*Zeng et al., 2019*).

This study integrates numerical simulation with experimental validation to develop an interaction model between a loading plate and straw–soil composites. The model quantifies the influence of varying straw contents on soil settlement and compressive stress, while explicitly elucidating the dual advantages of straw–soil mixtures: a marked reduction in both settlement and rut depth, thereby enhancing trafficability under wet field conditions, and a concomitant decrease in peak subsoil compaction stress, ultimately providing a theoretical foundation for alleviating soil compaction.

Theoretical analysis of soil compressive force

In previous studies on force transmission, the methods for calculating soil compressive force transmission have primarily relied on simulations and modeling. Existing analytical models assume that soil is a homogeneous, elastic, and isotropic medium (*Van Den Akker, 2004*). Considering soil as an elasto-plastic material (*Smith, et al., 2000*), *Boussinesq* in 1855 derived the compressive force formula for any point within an elastic soil subjected to a concentrated load:

$$\sigma_{zi} = \frac{3F}{2\pi R_i^2}\cos\theta_i \tag{1}$$

$$\sigma_x = \frac{3F}{2\pi}\left\{\frac{x^2 z}{R^5} + \frac{1-2\mu}{3}\left[\frac{1}{R(R+z)} - \frac{x^2(2R+z)}{R^3(R+z)^2} - \frac{z}{R^3}\right]\right\} \tag{2}$$

where: F represents the load at the soil surface loading point; σ_z and σ_x are the compressive force components in the z-axis and x-axis directions, respectively; R_i represents the horizontal distance from the point of concentration to the calculated point; θ_i is the angle between the line connecting the loading point and the prediction point and the vertical direction. R is the equivalent radius of the soil contact surface; x represents the horizontal distance from the point of concentration to the calculated point; z is the vertical distance between the loading point and the compressive force prediction point; μ is the Poisson's ratio of the soil. Due to significant discrepancies between the compressive force distribution predicted by the *Boussinesq* equation and the measured values (*Keller et al., 2004*), *Fröhlich et al., (1934*), modified the *Boussinesq* equation by introducing the "concentration coefficient v", resulting in compressive force values that better match actual observations. When determining the load at the soil surface loading point, the vertical compressive force σ_z at the point directly beneath the loading point (z) must be calculated as:

$$\sigma_z = -\frac{vF}{2\pi}\cdot\frac{z^v}{R^{v+2}} \tag{3}$$

In the vertical plane, the surface subjected to concentrated load is taken as the research object *(Xu, 2020*), as shown in Figure 1.

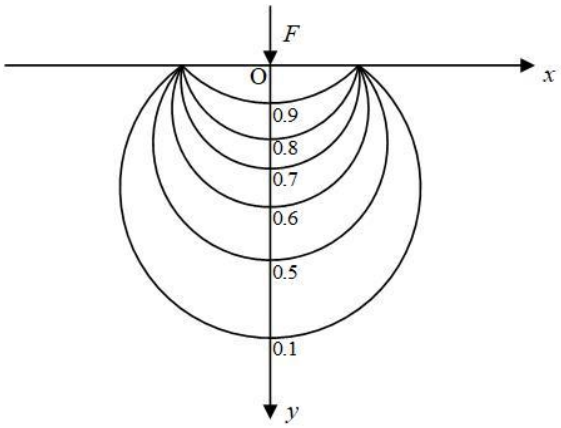

Fig. 1 - Compressive force field distribution in soil subjected to concentrated loads

As the force is transmitted downwards, the vertical compressive force on the surface of the soil layer significantly increases, with a rapid rate of increase. At the same time, soil particles, acting as a medium, effectively transfer the surface load to deeper soil layers. This force transmission mechanism holds significant theoretical and practical importance in soil mechanics. In the horizontal direction, as the position moves further from the applied force point O, the vertical compressive force σ_z decreases significantly, with the rate of decrease accelerating as the position approaches point O.

MATERIALS AND METHODS

Determination of soil wet bulk density and moisture content

Soil bulk density and gravimetric water content were determined using the core-cutter method. First, the sampling surface was leveled with a spade. A ring, pre-lubricated with Vaseline and placed on a previously weighed support, was pressed vertically into the soil until the ring was completely filled; three replicate cores were taken at each depth to ensure accuracy. Excess soil was trimmed flush with the knife edges at both ends, the outer wall of the ring was wiped clean, and the caps were fitted immediately to prevent moisture loss. Back in the laboratory, the combined mass of the soil-filled ring and the soil sample was weighed on a balance. The ring knife selected for the experiment is φ 79.8 mm × 20 mm, as shown in Figure 2.

The wet bulk density of each sample was then calculated using the following formula:

$$\rho_0 = \frac{m_1 - m_2}{V} \tag{4}$$

In the equation, ρ_0 denotes the wet bulk density of the soil specimen (g·cm^{-3}); m_1 represents the combined mass of the ring and the soil sample (g); m_2 corresponds to the mass of the empty ring (g); and V signifies the internal volume of the ring (cm³).

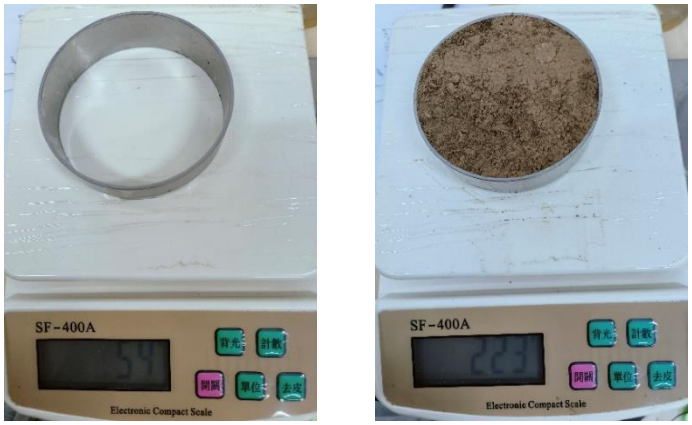

Fig. 2 - Wet density test of soil samples

Gravimetric soil water content (ω) was determined by the oven-drying method. After removing the ring cover, the soil sample was transferred into a pre-labelled aluminum box and weighed to obtain the tare mass of the box (m_3) and the combined mass of the box plus moist soil (m_4). The open box was then placed in a ventilated oven set at 105–110 °C and dried continuously for 6-8 h. Subsequently, the box was transferred to a desiccator to cool to room temperature and re-weighed until a constant mass (m_5, recorded to the nearest 1 g) was attained.

As shown in Figure 3, the gravimetric water content of the soil is calculated using the following equation:

$$\omega = \frac{m_4 - m_5}{m_4 - m_3} \times 100\% \tag{5}$$

The dry bulk density of the soil specimen, denoted ρ, is obtained as follows:

$$\rho = \frac{\rho_0}{1 + 0.01\omega} \tag{6}$$

(a) Soil drying

(b) Aluminum box weighing

(c) Weighing soil samples before drying

(d) Weighing soil samples after drying

Fig. 3 - Determination of water content of experimental soil samples

To ensure data reliability, each soil sample was tested in triplicate; the arithmetic mean of the three determinations was adopted as the definitive value for both bulk density and gravimetric water content. The resulting values are presented in Table 1.

Table 1

Bulk weight and water content of experimental soil samples

Soil name	Test count	Wet bulk density ($g \cdot cm^{-3}$)	Moisture content (%)	Dry bulk density ($g \cdot cm^{-3}$)	Average wet bulk density ($g \cdot cm^{-3}$)	Average moisture content (%)
Loam	1	1.7	19.41	1.70	1.807	19.73
	2	1.77	19.77	1.77		
	3	1.95	20	1.95		

Discrete Element Model of Soil Particles and Straw

In EDEM, discrete element simulations require the establishment of an appropriate DEM model, where the setting of material parameters is crucial. Based on references *(Ding, et al., 2017, Xiong, et al., 2018, Zhou, 2020*), the soil particle radius is set to 5 mm, and the Hertz-Mindlin with JKR contact model is applied, with a soil surface energy of 8.06 J/m². For the interaction between soil and geometry, the Hertz-Mindlin (no slip) contact model is used, and the gravitational acceleration is set to 9.81 m/s² along the negative Z-axis. The material parameters of the soil in the simulation are shown in Table 2. Straw is modeled as a long particle assembly composed of multiple particles, with the Hertz-Mindlin (no slip) contact model used to describe the interactions between straw particles. In this study, wheat straw is modeled as an assembly of six particles with a radius of 4 mm, arranged to form a length of 24 mm. Other straw parameters are referenced from relevant literature *(Zhang et al., 2018, Zhao et al., 2021*), as shown in Table 3.

The soil and straw particle models are depicted in Figure 4.

Table 2

Soil particle model simulation parameters

Parameters	Density ρ/kg·m^{-3}	Poisson's ratio *v*	Shear modulus *G* / MPa	Recovery coefficient *e*	Soil static friction coefficient μ_s	Soil dynamic friction coefficient μ_r	Soil moisture content / %
Value	1680	0.3	1	0.56	0.79	0.22	15

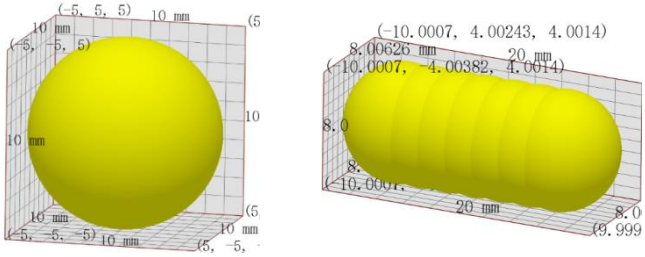

(a) Soil Particle Model **(b) Straw Pellet Model**

Fig. 4 - Soil and straw particle simulation models

Table 3

Straw pellet model parameters

Parameters	Value	Parameters	Value
Straw density *ρ*/ kg·m^{-3}	241	**Straw-soil static friction coefficient μ_s**	0.537
Particle radius *r*/ mm	4	**Straw-soil dynamic friction coefficient μ_r**	0.16
Number of particles	6	**Straw-straw recovery coefficient *e***	0.485
Straw Poisson's ratio *v*	0.4	**Straw-straw static friction coefficient μ_s**	0.213
Straw shear modulus *G*/ MPa	1	**Straw-straw dynamic friction coefficient μ_r**	0.098
Straw-soil recovery coefficient *e*	0.6		

Discrete Meta-Modelling of Straw-Soil Mixtures

To simulate the actual state of the straw-soil mixture, the simulation pressure chamber is set as a cylinder with a diameter of 150 mm and a height of 300 mm, with the model size being 60 times the soil particle radius. The soil is divided into two layers: the upper layer is a straw-soil mixture layer with a depth of 200 mm, and the lower layer is a pure soil layer with a depth of 100 mm. The particle generation process lasts for 3 seconds, with 0-2 seconds for particle generation and 2-3 seconds for settling and stabilization. In the final pure soil model, the total number of soil particles is 22,465. Mixed models are constructed according to the required straw content (volume ratio), with straw contents set at 20%, 30%, 40%, and 50%. Figure 5 shows the particle models for straw contents of 0, 30%, and 50%, which are used to analyze the effect of straw content on soil physical properties.

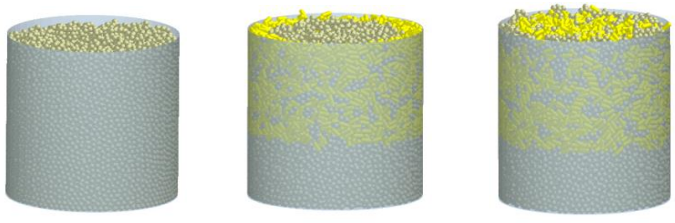

Straw content 0 Straw content 30% Straw content 50%

Fig. 5 - Straw-soil mixing model (yellow - straw, gray – soil)

RESULTS

Simulation Results and Discussion

Based on EDEM simulation software, this study established straw-soil mixing models with varying straw content, with a circular loading plate (radius 0.05 m, thickness 0.005 m) placed above the models. Pressure tests were conducted to simulate the dynamic interaction between the loading plate and the straw-soil mixture. In the first test scenario, a constant subsidence speed of 0.01 m/s (in the negative Z-axis direction) was applied to the loading plate, with a total simulation time of 3 seconds. This test analyzed the changes in particle movement and soil compressive force under different straw contents during the loading process. In the second test scenario, a constant load of 100 N was applied to the loading plate in the negative Z-axis direction, with the simulation time also set to 3 seconds. This test focused on the response of vertical force and soil subsidence at different depths of the model under varying straw contents over time. Based on the simulation results, the study explored the internal force transfer mechanism in the straw-soil mixture, focusing on the force transfer characteristics between straw and soil particles. The optimal loading conditions to alleviate soil compaction were determined, and the accuracy of the simulation model was validated through indoor experiments.

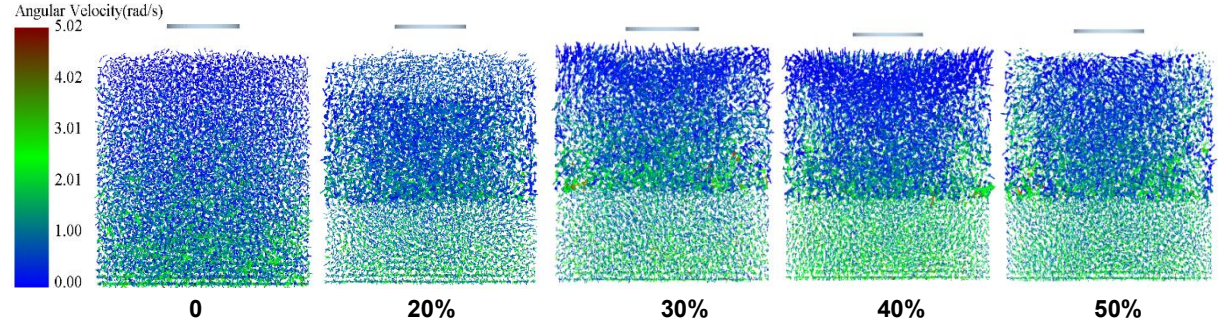

Fig.6 Plot of soil particle position change at 0s

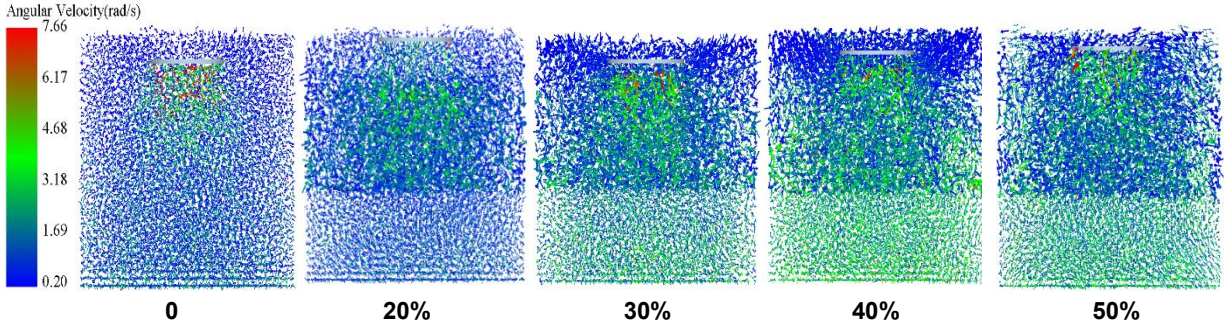

Fig. 7 - Change of soil particle position at 3s

Under the same sinking speed and the action of the loading plate, Figures 6 and 7 show the changes in the position of particles in the straw-soil mixture model with different straw contents. Initially, soil particles and straw move downward under the influence of gravity, with the loading plate not yet in contact with the soil surface. As the contact area increases, the movement of soil particles and straw undergoes significant changes, with vertical displacement extending deeper into the soil, leaving clear traces of the loading plate. As loading time increases, some particles begin to move laterally, and the soil and straw particles undergo settlement and movement under the loading plate's influence, being compressed and moving in other directions.

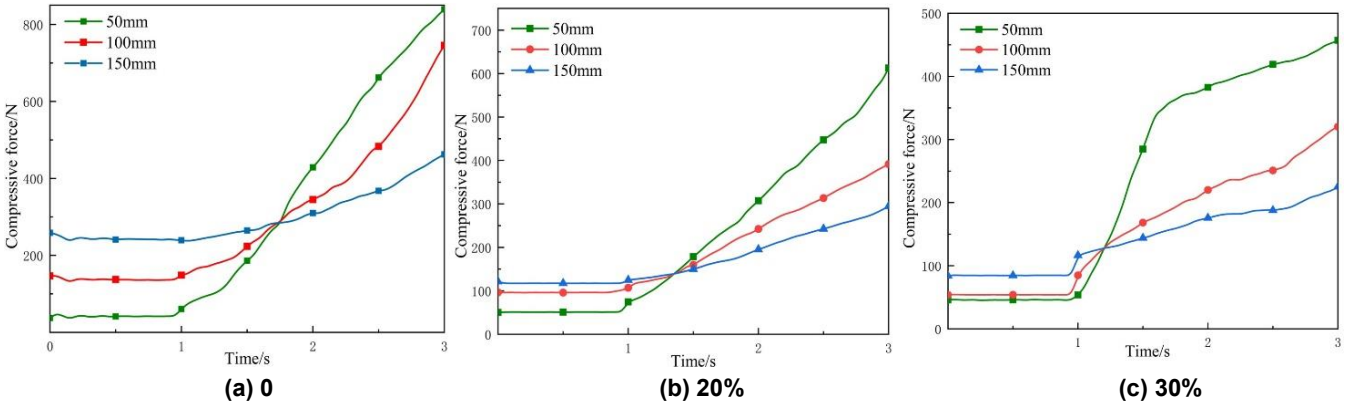

(a) 0 **(b) 20%** **(c) 30%**

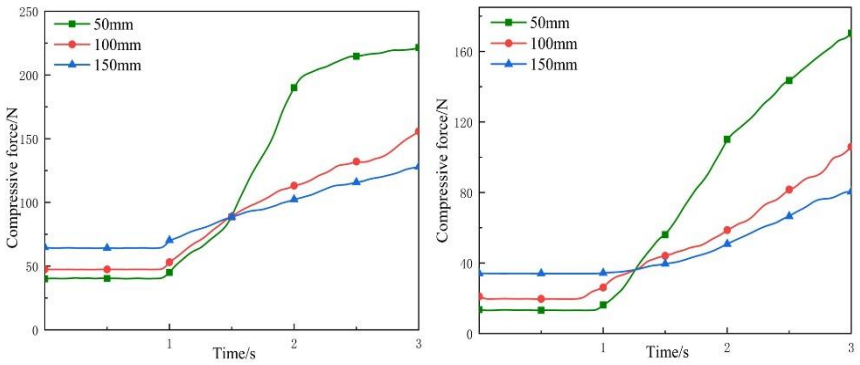

(d) 40% (e) 50%

Fig. 8 - Soil compressive force curve

Figure 8 illustrates the variation curves of soil compressive force under different straw contents. Figure 6(a) presents the compressive force variation in the pure soil model (0 straw content), where the compressive force is primarily generated by particle self-weight and collision-induced compression. After 1 second, the compressive forces at depths of 50 mm, 100 mm, and 150 mm all reached the pre-consolidation pressure and entered a stable phase. Figures 6(b) to 6(e) display the compressive force variations in straw-incorporated soil, all exhibiting typical three-stage characteristics: In the initial stage, the compressive force originates from soil self-weight and particle collisions; in the second stage (1-2 s), the compressive force increases slowly, with the intersection point of the curves representing the pre-consolidation pressure; in the third stage (2-3 s), the loading plate stress overcomes the "spring" effect of the straw. Data from Figure 6(e) show that at the 3-second mark, the compressive forces at 50 mm, 100 mm, and 150 mm depths in the 50% straw content model were 170.29 N, 105.91 N, and 80.43 N, respectively, representing reductions of 669.03 N, 639.79 N, and 382.04 N compared to the pure soil model.

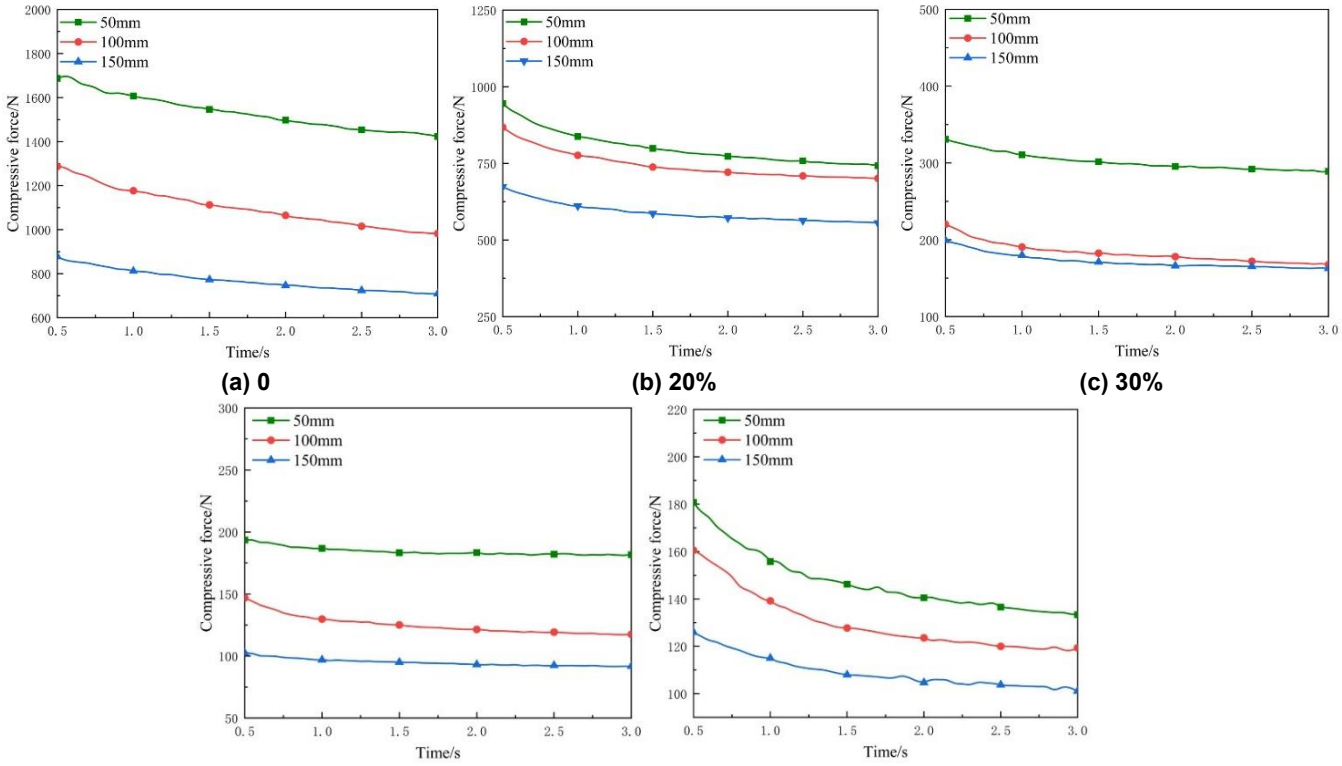

(a) 0 (b) 20% (c) 30%

(d) 40% (e) 50%

Fig. 9 - Soil compressive force curves at different depths under identical loading plate conditions

Figure 9 illustrates the variation of soil compressive force with time at different depths under the same load. Figure 9(a) describes the change in soil compressive force over time after the loading plate is applied to pure soil, while Figures 9(b) to (e) show the dynamic changes in soil compressive force when the straw content is 20%, 30%, 40%, and 50%, respectively.

Comparisons reveal that for the same straw content, the soil compressive force decreases gradually over time. One second after the load is applied, the soil compressive force begins to decline progressively. In Figure 9(e), for the model with a straw content of 50%, the compressive force values at depths of 50 mm, 100 mm, and 150 mm are 133.34 N, 119.33 N, and 101.09 N, respectively. Compared with the pure soil model in Figure 9(a), these values are reduced by 1289.36 N, 862.9 N, and 607.49 N, respectively. Thus, at the same depth, the soil compressive force decreases with increasing straw content. This phenomenon occurs because the addition of straw alters the contact area between soil particles and transfers part of the applied pressure to the underlying soil. As the straw content increases, more of the applied load is transferred to the straw particles. The larger surface area of the straw increases the contact area between particles, thereby reducing the pressure on the underlying soil.

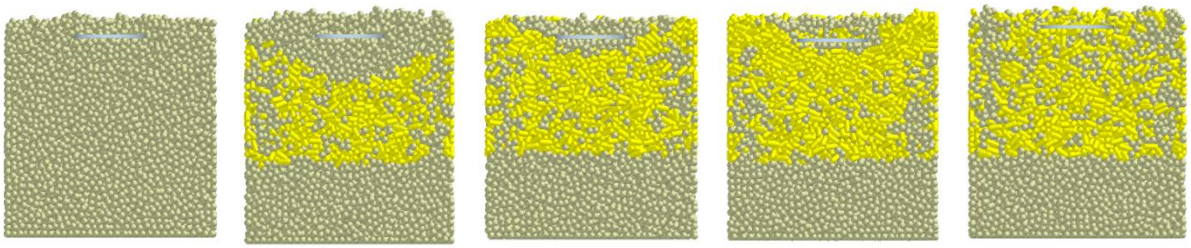

0 20% 30% 40% 50%

Fig. 10 - Soil subsidence response to different straw contents under the same loading stress

Table 4

Changes in the amount of sedimentation of discrete soil particles

Straw content	0	1	2	3	4	5	Average value/mm
0	0	25.62	24.91	26.47	23.86	24.55	25.082
20%	0	24.93	24.55	25.17	25.04	24.87	24.912
30%	0	24.89	24.67	25.23	24.52	24.69	24.8
40%	0	23.98	24.14	24.20	23.81	23.94	24.014
50%	0	21.75	20.63	20.79	21.29	21.47	21.186

The effect of straw content on the soil's discrete settlement under the same loading plate stress is shown in Figure 10. To minimize measurement errors, five points were selected for settlement measurement on the straw-soil mixed model with different straw contents (as shown in Table 4), and the average value of five measurements was taken. The results indicate that the settlement values for straw contents of 0, 20%, 30%, 40%, and 50% are 25.082 mm, 24.912 mm, 24.8 mm, 24.014 mm, and 21.186 mm, respectively. It can be observed that at 50% straw content, the settlement is reduced by 3.896 mm compared to pure soil. This phenomenon can be explained by the cohesive nature of the soil (*Arabani, et al., 2023, Xue, et al., 2024*). The soil structure has shear resistance, while straw possesses tensile strength, and there is frictional resistance between soil particles and straw particles. The straw is randomly distributed within the soil structure, forming a network-like supporting structure that enhances the stability of the soil, thereby alleviating the settlement tendency of the soil (*Bahrami, et al., 2022*).

Experimental Results and Discussion

In this experiment, the soil samples were taken from the plow layer (0-10 cm depth) of the experimental field, as shown in Figure 11. The straw used in the experiment was cut to a length of 5 cm, as shown in Figure 12. A WG-type single-lever consolidation apparatus (medium and low pressure), produced by Nanjing Soil Instrument Factory Co., Ltd., was used to perform uniaxial compression tests on the soil samples, as shown in Figure 13. The NSIF geotechnical testing control data acquisition system was employed to monitor deformation and pressure changes during the soil compaction process, and to evaluate the relationship between porosity and applied pressure after compaction, as well as the change in sample height. A soil sample container with an area of 50 cm² was used, and a loading plate with a diameter of 8 cm was applied to the sample at a pressure of 25 kPa. The experiment was repeated five times, and the average value was taken. The data acquisition system was used to analyze the porosity-load (*e-p*) curves for soil samples with different straw contents and to measure the settlement after soil compaction. The relevant results are shown in Figure 14, Figure 15, Figure 16 and Table 5.

Fig. 11 - Soil sample

Fig.12 - Straw sample

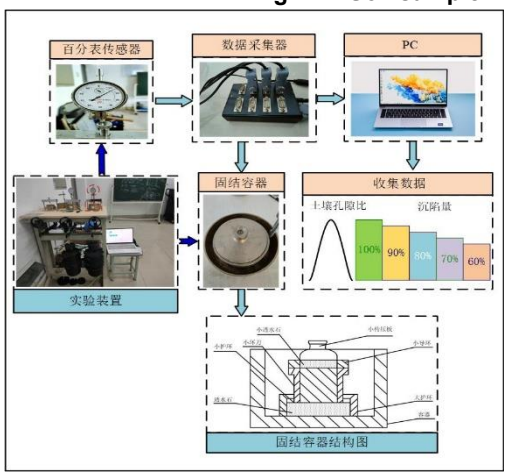

Fig. 13 - WG type single lever consolidation meter

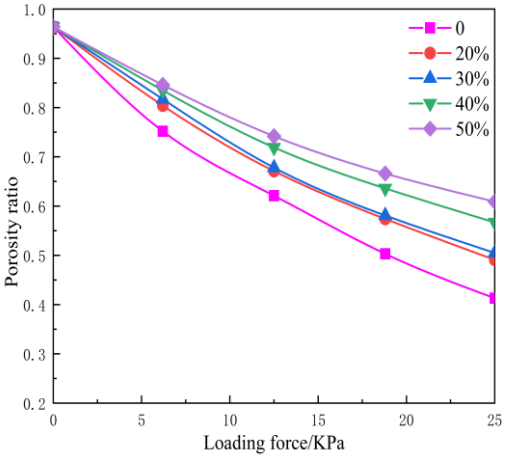

Fig. 14 - Pore ratio versus loading force curve

The response of soil void ratio to different straw contents under the same loading plate stress is shown in Figure 12. In discrete element numerical simulations, particles were scaled up to more efficiently simulate soil particle behavior. Although this scaling might result in slightly higher void ratio values in the simulation compared to actual compaction conditions, the focus of this study is on the trend of void ratio changes after compaction rather than the exact numerical values. As shown in Figure 14, under the same vertical load, the void ratio of straw-soil mixtures with different straw contents increases with higher straw content during compression. When the loading plate applies a stress of 25 kPa, it is observed that the void ratio of pure soil is reduced by 0.196 compared to the straw-soil mixture with 50% straw content.

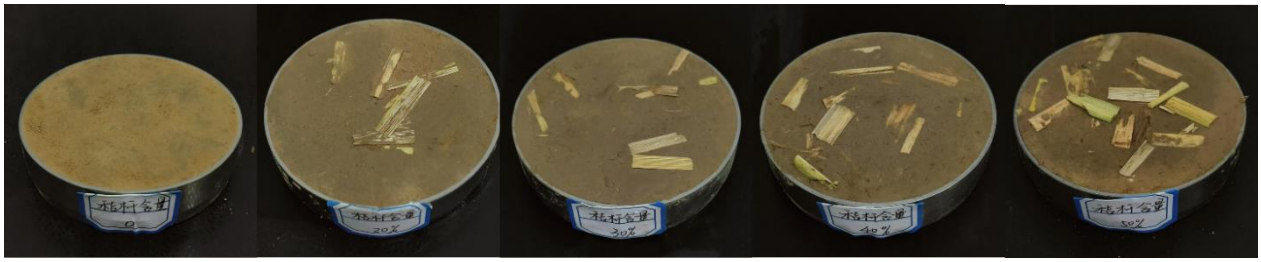

0 20% 30% 40% 50%

Fig. 15 - Soil samples with different straw contents prior to the application of load

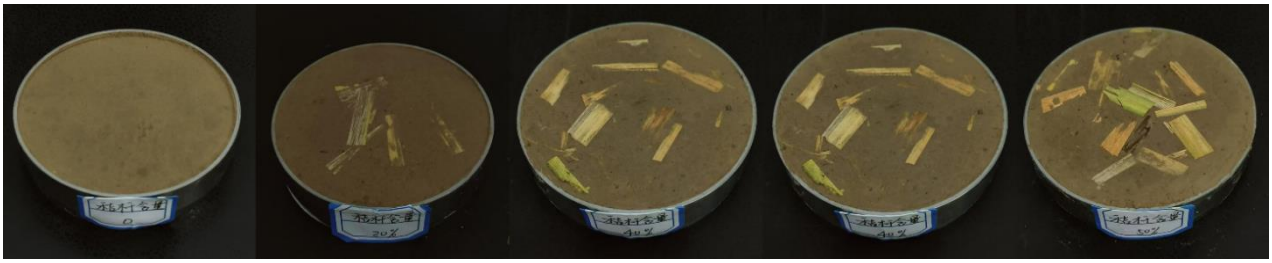

0 20% 30% 40% 50%

Fig. 16 - Soil samples with different straw contents after the application of load

Table 5

Changes in soil particle subsidence

Straw content	0	1	2	3	4	5	Average value/mm
0	0	5.611	5.634	5.619	5.689	5.674	5.6454
20%	0	4.823	4.821	4.840	4.877	4.811	4.8344
30%	0	4.674	4.665	4.689	4.711	4.653	4.6784
40%	0	4.045	4.099	4.057	4.059	4.042	4.0604
50%	0	3.616	3.625	3.620	3.618	3.612	3.6182

Figure 15 and Figure 16 comparatively analyzed the morphological changes of soils with different straw contents before and after the application of external loads. In the initial state, the structure of each soil sample was intact, with uniformly distributed pores, and no significant macroscopic morphological differences were observed due to the variation in straw content. However, after the application of external loads, the deformation behavior of the soil exhibited distinct differentiation: pure soil, due to its insufficient organic matter, experienced increased contact stress between particles, resulting in significant compressive settlement. In contrast, with the increase in straw content, the pore structure remained stable due to the mesh-like supporting effect of straw fibers, and the settlement was significantly reduced. The pure soil sample demonstrated typical overall plastic deformation, while the straw-amended soil samples exhibited localized deformation characteristics, with an elastic rebound zone forming at the fiber-soil interface, which validated the “micro-spring” effect of the straw reinforcement. This phenomenon is consistent with the experimental data in Table 5, which shows that the settlement of the sample with 50% straw content decreased by 2.0272 mm.

Under the same loading plate stress conditions, the response of soil particle settlement to different straw contents is presented in Table 5. A comparison between Table 4 and Table 5 reveals that the increase in straw content significantly reduces the soil settlement, and this trend is consistent in both simulation and experimental results. As the straw content increases from 0 to 50%, the settlement decreases by 3.896 mm in the simulation and by 2.0272 mm in the experiment, showing an overall decreasing trend.

Numerical simulations confirm the “micro-spring” effect of straw via the elastic modulus, and experimental studies show that the smooth straw surface markedly reduces inter-particle friction and cohesion (*Meena et al., 2021*). This behavior endows straw-amended soil with two practical advantages when agricultural vehicles pass: it decreases soil settlement and wheel rut depth, thereby improving trafficability on wet fields, and it also lessens the peak compaction stress on deeper layers, preserving soil aggregate structure and diminishing the need for subsequent tillage.

CONCLUSIONS

This study is based on soil compaction issues and uses a combination of discrete element numerical simulation and indoor experiments to systematically investigate the effects of different straw contents (0–50%) on soil compaction characteristics. The main conclusions are as follows:

1. In pure soil without straw, the overall movement of particles is mainly manifested as vertical displacement, leaving obvious traces on the surface. As the straw content increases, the proportion of lateral particle movement gradually increases.

2. Discrete element simulation and indoor experimental results indicate that, at a constant velocity, the compressive force of a mixture containing 50% straw decreases by approximately 27%, 25%, and 22% at depths of 50 mm, 100 mm, and 150 mm, respectively, compared to pure soil; under constant load conditions, the compressive force decreases by approximately 32%, 29%, and 28%, respectively. Soil settlement decreases with increasing straw content. The maximum settlement values in the simulation and experiments were 25.082 mm and 4.834 mm, respectively, while the minimum settlement values were 21.186 mm and 3.618 mm, respectively. The porosity of pure soil is 0.196 lower than that of the straw-soil mixture with 50% straw content. This validates the “micro-spring” effect of straw, which increases the contact area between particles, distributes the load, and effectively enhances the soil's compressive strength.

Therefore, straw-soil mixtures can effectively alleviate soil compaction caused by agricultural machinery operations by optimizing soil pore structure and improving compressive strength. They can also improve the passability of agricultural machinery in wet fields.

ACKNOWLEDGEMENT

This study was supported by the National Natural Science Foundation of China - Young Scientists Fund (Grant No. 52105239). We would like to thank Editage for providing English language editing services. We also appreciate the editor and anonymous reviewers for their valuable suggestions, which helped improve the quality of this paper.

REFERENCES

[1] Abdeldayem M A., Tekeste M Z. (2025), Multiresponse optimization of DEM Elasto-plastic model for soil-to-bulldozer blade interaction. *Powder Technology*, Vol.460, pp.121056, USA.

[2] Arabani M., Shalchian M M., Rahimabadi M M. (2023), The influence of rice fiber and nanoclay on mechanical properties and mechanisms of clayey soil stabilization. *Construction and Building Materials*, Vol. 407, pp. 133542, Iran.

[3] Bahrami M., Naderi-Boldaji M., Ghanbarian D., Keller T. (2022), Simulation of soil stress under plate sinkage loading: A comparison of finite element and discrete element methods. *Soil and Tillage Research*, Vol. 223, pp. 105463. Iran.

[4] Ding Q ., Ren J., Adam B E., Zhao J ., Yang G ., Yang L. (2017), DEM Analysis of Subsoiling Process in Wet Clayey Paddy Soil (湿粘水稻土深松过程离散元分析). *Nongye Jixie Xuebao*, Vol.48, pp. 38-48. Jiangsu/China.

[5] Fröhlich A., Zak E. (1934), Der Einfluß verschiedener Pharmaca auf die Herzwirkung des Kristallvioletts. *Archiv f. experiment. Pathol. u. Pharmakol*, Vol. 177, pp. 103-112, Germany.

[6] Gheshlaghi F., El-Sayegh Z., Sharifi M., El-Gindy M. (2020), Prediction and validation of terramechanics models for estimation of tyre rolling resistance coefficient. *International Journal of Vehicle Systems Modelling and Testing*, Vol. 14, pp. 71-82, Iran.

[7] Hamza M., Anderson W K. (2005), Soil compaction in cropping systems: A review of the nature, causes and possible solutions. *Soil and tillage research*, Vol. 82, pp. 121-145. Australia.

[8] Jjagwe P., Tekeste M Z., Alkhalifa N., Way T R. (2023), Modeling tire-soil compression resistance on artificial soil using the scaling law of pressure-soil sinkage relationship. *Journal of Terramechanics*, Vol.108, pp. 7-19, USA.

[9] Keller T., Arvidsson J. (2004), Technical solutions to reduce the risk of subsoil compaction: effects of dual wheels, tandem wheels and tyre inflation pressure on stress propagation in soil. *Soil Tillage Res*., Vol.79, pp.191-205, Sweden.

[10] Meena S.K., Sahu R., Ayothiraman R. (2021), Utilization of waste wheat straw fibers for improving the strength characteristics of clay. *Journal of Natural Fibers*, Vol. 18, pp. 1404-1418, India.

[11] Moslem N., Hossein G. (2014), Numerical simulation of tire/soil interaction using a verified 3D finite element model. *Journal of Central South University*, Vol. 21, pp. 817-821. Iran.

[12] Smith R., Ellies A., Horn R. (2000), Modified Boussinesq's equations for nonuniform tire loading. *Journal Terramech*., Vol. 37, pp. 207-222, Germany.

[13] Van Den Akker J J H. (2004), SOCOMO: a soil compaction model to calculate soil stresses and the subsoil carrying capacity. *Soil Tillage Res*., Vol. 79, pp. 113-127, Netherlands.

[14] Xiong P ., Yang Z., Sun Z ., Qian Z ., Qing H ., Wei Z . (2018), Simulation analysis and experiment for three-axis working resistances of rotary blade based on discrete element method (基于离散元法的旋耕刀三向工作阻力仿真分析与试验). *Transactions of the Chinese Society of Agricultural Engineering*, Vol.34, pp. 113-121. Guangdong/China.

[15] Xu J. (2020), Research of Farmland Multidirectional Wireless Earth Pressure Sensor and Monitoring System (农田多向无线土压力传感器及监测系统的研究) [D]. *Northeast Agricultural University*, Beijing/China.

[16] Xue M., Zhang J., Xu G. (2024), Study on Strength of Slip Soil–Tuff Contact Surfaces in Tuff Landslide Based on Model Test (基于模型试验的凝灰岩滑坡滑移土-凝灰岩接触面强度研究). *Applied Sciences*, Vol.14, pp.1687. Hubei/China.

[17] Zeng Z., Chen Y. (2019), Simulation of straw movement by discrete element modelling of straw-sweep-soil interaction. *Biosystems Engineering*, Vol. 180, pp.25-35. Canada.

[18] Zhang T., Liu F., Zhao M., Ma Q., Wang W., Fan Q., Yan P. (2018), Determination of corn stalk contact parameters and calibration of Discrete Element Method simulation (玉米秸秆接触物理参数测定与离散元仿真标定). *Journal of China Agricultural University*, Vol. 23, pp. 120-127. Beijing/China.

[19] Zhao S ., Liu H ., Yang C., Yang L., Gao L ., Yang Y . (2021), Design and Discrete Element Simulation of Interactive Layered Subsoiler with Maize Straw Returned to Filed (玉米秸秆还田交互式分层深松铲设计与离散元仿真). *Nongye Jixie Xuebao*, Vol. 52, pp. 75-87. Jilin/China.

[20] Zhou H. (2020), Experimental and simulation study on combined tillage machine for deep rotary burying of straw incorporation into soil in rice-rape rotation area (稻油轮作区秸秆深埋复式耕作机试验与仿真研究) [D]. Wuhan: *Huazhong Agricultural University*, Hubei/China.